Calculation of the Two-Phase Aft-Dome Flowfield in Solid Rocket Motors

Ravi K. Madabhushi,* Jayant S. Sabnis,† Frederik J. de Jong,‡ and Howard J. Gibeling§
Scientific Research Associates, Inc., Glastonbury, Connecticut 06033

The two-phase flowfield in the aft-dome region of a solid rocket motor (SRM) with submerged nozzle has been simulated using a combined Eulerian-Lagrangian analysis. This analysis uses the numerical solution of ensemble averaged Navier-Stokes equations for the continuous (gas) phase coupled with a Lagrangian analysis for the discrete (particulate) phase to simulate the two-phase internal flow. A linearized block-implicit (LBI) scheme is used to solve the governing equations for the continuous phase, which allows the use of a highly stretched grid with sublayer resolution. The motion of the particles is tracked in computational coordinate space resulting in computational efficiency, and the interphase coupling terms for the Eulerian analysis are computed from the instantaneous distribution of the particles. A low Reynolds number form of the k-ϵ turbulence model is used with modifications for injection driven flows. Calculations have been performed for a particular grain configuration of the Space Shuttle SRM. The flowfield in the vicinity of the submerged nozzle, the particle trajectories, and the sensitivity of two-phase effects (such as slag accumulation) to the particle injection parameters are presented in this paper.

Nomenclature

C_D = drag coefficient
D = diameter
e_ℓ = internal energy of discrete phase droplets
F_D = interphase drag per unit volume acting on the gas phase
F_p = drag force on a particle
g = vector sum of gravitational acceleration and motor acceleration
h = enthalpy
h_{fg} = latent heat of vaporization
$[J]$ = Jacobian matrix of coordinate transformation
k = turbulent kinetic energy
m = mass
$\dot{m}_v$ = rate of mass addition per unit volume to gas phase
p = pressure
q = heat flux vector in the continuous phase
$\dot{q}_v$ = rate of interphase heat exchange per unit volume
Re = Reynolds number
t = time
U = velocity
u_i' = turbulent velocity component
X = position vector in physical space
x_i = component of the position vector in physical space
Y = position vector in coordinate space
y^j = component of the position vector in coordinate space
α = void fraction
ϵ = turbulence dissipation
Δt_s = subtime step
μ = continuous phase viscosity
ρ = density
τ = stress tensor
Φ = viscous dissipation

Subscripts
p = particle
v = per unit volume
R = relative

Introduction

THE flowfield in the aft dome of a solid rocket motor (SRM) has a significant impact on the operation of the motor as well as its performance. The pressure distribution in this region influences the design requirements of the nozzle-to-case joint, and the shear layer structure determines the heat transfer rates and thus determines the requirements of the liner design. The interaction between the particulate phases and the nozzle inlet section determines the slag accumulation rate and thus affects the nozzle erosion and motor performance. Accurate prediction of the flowfield in the aft-dome region is therefore of significant importance in the design of SRMs. Analysis of the aft-dome flowfield using the techniques of computational fluid dynamics (CFD) provides an excellent means of evaluating the effects of phenomena such as motor acceleration, which are not otherwise measurable through static motor tests.

The flowfield in the vicinity of the submerged nozzle region is of a complex nature due to the presence of the cavity. The flow in the aft-dome chamber is turbulent, whereas the flow in the cavity is laminar with possible recirculation regions. Predictive techniques used commonly at present involve the use of inviscid methods with boundary-layer corrections to the mean flow estimated iteratively and require the division of the flow into an inviscid region and a boundary layer. In the vicinity of the submerged nozzle such a division is not possible, and the boundary-layer approximations are not valid. Hence, a more general approach for flow prediction is needed. Numerical solution of the ensemble-averaged Navier-Stokes equations was employed by Sabnis et al.[1] to provide such a general approach to simulate SRM internal flows. The only approximations involved in this approach are those of Newtonian fluid mechanics and the turbulence model. This scheme, along with a modified low Reynolds number form of the k-ϵ turbulence model (see Sabnis et al.[2]), was used in the present study to simulate the gas phase flowfield. The use of the low Reynolds number form of the k-ϵ turbulence model eliminates the need for using the "wall function" approach, which would be questionable for this flowfield.

Presented as Paper 89-2780 at the AIAA/ASME/SAE/ASEE 25th Joint Propulsion Conference, Monterey, CA, July 10–12, 1989; received Sept. 15, 1989; revision received Feb. 18, 1990; accepted for publication March 2, 1990.

*Associate Research Scientist; currently at Department of Mechanical Engineering, University of Illinois at Urbana-Champaign.
†Senior Research Scientist. Member AIAA.
‡Research Scientist. Member AIAA.
§Assistant Vice-President. Member AIAA.

The motion of the particulate phase was described in the Lagrangian reference frame using the approach of Sabnis et al.[3] Here the particulate motion is simulated using "computational particles" (discussed later) under the influence of the local environment produced by the continuous phase; the interphase coupling terms for the continuous phase equations are computed from the instantaneous distribution of the particles. The motion of the particles is tracked in computational space, which results in computational efficiency. The particulate phase attributes (such as the position and velocity vectors, size, temperature, etc.) are updated along the trajectories. This approach can easily accommodate changing particle size as well as a range of particle sizes without any significant increase in computational effort, because the particle size is simply one of the attributes of the particulate phase. The two-phase flow is simulated by combining the solution of the ensemble-averaged Navier-Stokes equations including the interphase coupling terms for the continuous phase with the Lagrangian description for the particulate phase. Such a combined Eulerian-Lagrangian analysis has been successfully used by Sabnis et al.[3] in the computation of two-phase shear layer flow in a two-dimensional channel flow configuration, and by de Jong et al.[4] in the analysis of Space Shuttle main engine high pressure oxidizer turbo pump (SSME HPOTP) nozzle plug trajectories. This analysis is extended here to simulate the two-phase flowfield in the aft-dome region of an SRM with submerged nozzle.

Analysis and Governing Equations

The combined Eulerian-Lagrangian multidimensional implicit Navier-Stokes time-dependent code (CELMINT) used in the simulation of the two-phase flow in the submerged nozzle region involves the solution of the ensemble-averaged Navier-Stokes equations for the continuous phase with interphase mass, momentum, and energy source terms computed from the Lagrangian particle transport calculations. The equations to be solved for the continuous phase are the mass, momentum, energy conservation, and they are written as follows:

$$\frac{\partial(\alpha\rho)}{\partial t} + \nabla\cdot(\alpha\rho U) = \dot{m}_v \tag{1}$$

$$\frac{\partial(\alpha\rho U)}{\partial t} + \nabla\cdot(\alpha\rho UU) = -\nabla(\alpha p) + \nabla\cdot\alpha\tau + \dot{m}_v U_p + F_D \tag{2}$$

$$\frac{\partial(\alpha\rho h)}{\partial t} + \nabla\cdot(\alpha\rho Uh) = \frac{D(\alpha p)}{Dt} + \alpha\Phi - \nabla\cdot\alpha q + \dot{q}_v - U_R\cdot F_D + \dot{m}_v(h_{fg} + e_\ell + \tfrac{1}{2}U_R\cdot U_R) \tag{3}$$

Here, U_p is the particle velocity and U_R ($= U-U_p$) is the velocity of the continuous phase relative to the discrete phase. It should be noted that all of the discrete phase interchange terms (i.e., $\dot{m}_v$, $\dot{m}_v U_p$, F_D, $\dot{q}_v$, etc.) and the void fraction α in the preceding equations are computed for each Eulerian cell by summation of the appropriate quantities over *all* of the computational particles within the cell.

In addition to the interphase mass, momentum, and energy transfer source terms appearing in Eqs. (1-3), relations are required for the stress tensor τ (including a turbulence model), dissipation Φ, and heat flux vector q. An equation of state relating the pressure, density, and temperature, and a caloric equation of state relating enthalpy and temperature are also needed. These auxiliary equations have been listed by Sabnis et al.[5] The turbulence model used is the low Reynolds number k-ϵ turbulence model of Jones and Launder[6] with the modifications proposed by Sabnis et al.[2] for use in computation of injection-driven flows. These modifications utilize a parameter v_w^+, which is the ratio of the injection velocity (v_w) to the "friction velocity" ($u^* = [\tau_w/\rho]^{1/2}$) as similarity parameter in characterizing the relative dominance of the injection effects vs the boundary-layer effects. Using this parameter, the "low Reynolds number" terms of the k-ϵ model have been modified. Further, this parameter is used in evaluating the turbulence kinetic energy and length scale at the porous surface. The preceding equations are solved using a consistently split, linearized block-implicit (LBI) scheme developed by Briley and McDonald.[7] The solution procedure treats the nonlinearities noniteratively by Taylor series linearization and then splits the matrix into a series of easily solved block-banded subsystems. The solution algorithm is computationally efficient and found to be rapidly convergent. Details of the stability and convergence rate of the algorithm have been discussed by Briley and McDonald.[7]

The interphase source terms in the continuous phase governing equations are obtained from the discrete phase analysis. A discrete particle model utilizing the Lagrangian description of the motion of computational particles is used for the discrete phase analysis. Each computational particle represents a collection of physical particles that have the same attributes, i.e., spatial location, velocity, mass, size, composition, temperature, etc. The equations of motion for a particle can be written as

$$\frac{d^2X}{dt^2} = \frac{1}{m}F_p + g \tag{4}$$

A coordinate transformation is introduced to transform the physical coordinates x_i into the computational coordinates y^j that correspond to the Eulerian analysis for the continuous phase,

$$y^j = y^j(x_1, x_2, x_3) \tag{5}$$

The equation of motion of the particle can then be integrated and transformed to yield

$$\frac{dY}{dt} = [J]\left\{\int_{t_1}^{t_1+\Delta t_s}\frac{1}{m}F_p\,dt + g\Delta t_s + \left.\frac{dX}{dt}\right|_{t_1}\right\} \tag{6}$$

where

$$[J] = \frac{\partial(y^1, y^2, y^3)}{\partial(x_1, x_2, x_3)}$$

is the Jacobian matrix for the transformation and Δt_s is a suitably chosen integration subtime step. Equation (6) can therefore be integrated to yield (assuming $[J]$ and F_p do not change over the integration interval)

$$\Delta Y = [J]\left\{\frac{1}{m}F_p + g\right\}\frac{\Delta t_s^2}{2} + [J]\left.\frac{dX}{dt}\right|_{t_1}\Delta t_s \tag{7}$$

which allows tracking of the particle motion in computational coordinate space and is thus computationally efficient. The details of this approach can be found in Ref. 3.

In the present calculations, the drag force on the particles, F_p, was evaluated using commonly used empirical correlations, specifically,

$$F_p = \frac{1}{8}C_D\rho\pi D_p^2\,|U_R|U_R \tag{8}$$

where D_p is the particle diameter and C_D is the drag coefficient given by

$$C_D = \begin{cases}\dfrac{24}{Re_p}\left(1+\dfrac{1}{6}Re_p^{2/3}\right) & ;\ Re_p < 1000\\ 0.424 & ;\ Re_p \geq 1000\end{cases} \tag{9}$$

The particle Reynolds number Re_p is given by

$$Re_p = \frac{\rho U_R D_p}{\mu} \tag{10}$$

Discrete Phase Turbulent Dispersion

In two-phase flows, the continuous phase turbulence results in dispersion of the discrete phase. This process has been modeled by some researchers (see, for example, Abbas et al.[8]) by adding a "diffusion" velocity obtained from some phenomenological model to the particle velocity. In the present effort, the turbulent dispersion of the discrete phase was modeled by subjecting the particles to an instantaneous velocity field of the continuous phase rather than its mean velocity field. The continuous phase turbulence was assumed to be isotropic, and the random turbulent velocity components were assumed to have a Gaussian probability distribution with standard deviation equal to $(2/3k)^{1/2}$. Similar techniques have been used by, for example, Dukowicz[9] and Gosman and Ioannides.[10] The turbulent velocity components are thus computed using

$$u_i' = \left(\frac{4k}{3}\right)^{1/2} erf^{-1}(2x-1) \tag{11}$$

where x is a random variable with uniform probability distribution between 0 and 1. The stochastically generated turbulent velocity components are added to the mean velocity field of the continuous phase in evaluating the interphase drag force.

Application and Results

This combined Eulerian-Lagrangian analysis, incorporated into the code CELMINT, was used in the present effort to simulate the two-phase flowfield in the submerged nozzle region of the Space Shuttle SRM at the initial grain and the 19-s grain burnback configurations. The flow was assumed to be axisymmetric, which is a reasonable assumption (when the nozzle is not canted) since any circumferential variations caused by the star-grain at the head end are not likely to be strong at the aft end for this motor. The simulation procedure consisted of first obtaining the steady state flowfield for the continuous phase. The particulate phase was then injected into the domain at the propellant surface and at the inlet, and the calculation procedure was continued to obtain a steady-state two-phase flowfield.

The geometric details and the grain surface corresponding to 19-s burnback were obtained from the engineering drawings for a 7.5% scale model in use at NASA Marshall Space Flight Center. A schematic diagram of the computational domain used in the present calculation is shown in Fig. 1. For the initial time configuration, the propellant grain surface lies below the nozzle entrance (lip), whereas for the 19-s burnback configuration, the grain surface lies above the nozzle entrance. Thus the particles in the chamber core as well as those close to the walls are unlikely to enter the submerged nozzle cavity for the initial time grain configuration, whereas for the 19-s burnback configuration, some of the particles are likely to accumulate in the cavity. The single-phase calculations appear to support this assumption, as will be seen later. Hence, the two-phase calculations were performed only for the 19-s burnback grain configuration.

The inflow and outflow boundaries were located sufficiently far away from the submerged nozzle region to minimize the effect of the assumptions/approximations made in the implementation of the boundary conditions there. The inflow boundary was located approximately 2 diameters upstream of the aft dome. The outflow boundary was in the diverging section of the nozzle where the flow is supersonic. The computational grid for this complex geometry was generated using EAGLE, the elliptic grid generation code of Thompson.[11] The grid distribution along the boundaries was obtained using the technique of Oh.[12] The computational grid consisted of 66 radial points in the chamber and nozzle and 190 points in the axial direction. There were 45 radial and 50 axial points inside the cavity. The grid distribution was so chosen as to resolve the sublayers in near-wall regions. The computational grid used in the present calculations is shown in Fig. 2, and the details of the grid near the nozzle cavity are presented in Fig. 3.

The flow conditions and the boundary conditions used are briefly described in the following. The propellant burning rate was assumed to be 19.28 kg/m^{2}s (computed from the propellant density and grain regression rate data), and the nominal chamber pressure and gas temperature were assumed to be 4.829 MPa (700 psia) and 3400 K, respectively. The mass flow at the inflow boundary was computed from the propellant burning rate and the grain surface area upstream of the the inflow boundary. For this mass flow at the inlet, an equivalent stagnation pressure at the centerline was computed assuming that the velocity profile is given by the analysis of Culick.[13] At the inflow boundary, normalized velocity profiles were specified and the static pressure was linearly extrapolated. The centerline axial velocity magnitude was computed from the stagnation pressure at the centerline and the local static pressure. At the propellant grain surface, a specified uniform mass flux rate was used as the boundary condition. At the propellant surface and the inflow boundary, the total temperature of the gas was specified and the inert surfaces (such as the nozzle walls, etc.) were assumed to be adiabatic. The boundary conditions used at the outflow boundary (i.e., nozzle exit plane) consisted of linear extrapolation of the dependent variables, consistent with the characteristics in a supersonic flow. At the centerline, symmetry boundary conditions were used for all the dependent variables.

For two-phase calculations, the particulate phase was injected at the propellant surface and the inflow boundary. In the present study, the particulate phase was assumed to be aluminum oxide (Al_2O_3); thus no attempt was made to simulate the combustion of aluminum. The aluminum oxide in the solid rocket motors has been known to exhibit a bimodal size distribution (see Price[14]). The small size mode corresponds to micron-sized Al_2O_3 "smoke," and the large size mode corresponds to Al_2O_3 "agglomerates," which are two orders of magnitude larger in size than the smoke particles. The mass-mean diameter for each mode as well as the Al_2O_3 mass split between the two modes would depend on the particular pro-

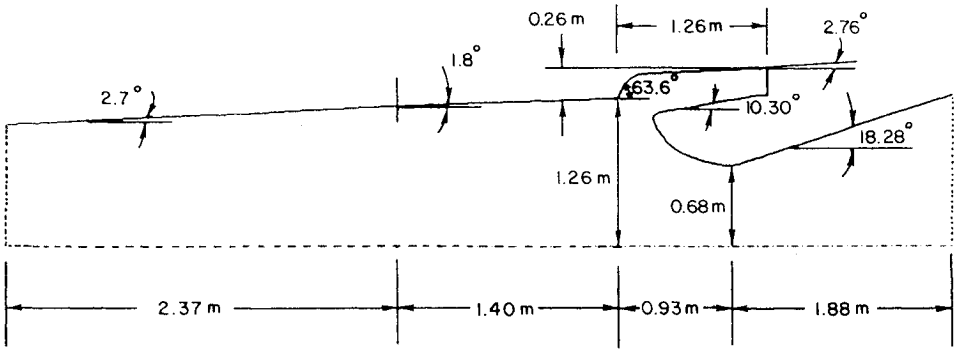

Fig. 1 Schematic diagram of the computational domain for 19-s burnback configuration.

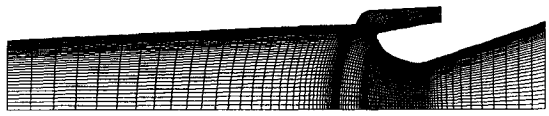

Fig. 2 Computational grid for 19-s burnback configuration.

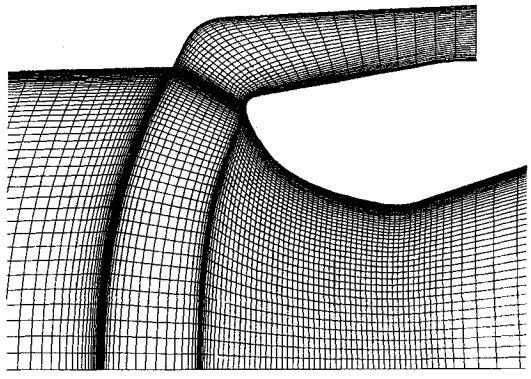

Fig. 3 Details of the computational grid near the nozzle cavity.

pellant formulation and the motor. In the present study, the Al_2O_3 smoke was included with the continuous phase, and the particulate phase was assumed to consist only of Al_2O_3 agglomerates. The mass fraction of the particulate phase was assumed to be 7.8% of the mixture, and the density of the particles was assumed to be 2211 kg/m^3. The size distribution of the particles was assumed to be log-normal with a mass-mean diameter of 150 μm and a standard deviation of 0.2. Thus the actual size of the particles injected at a grid point was obtained from the preceding distribution using a random variable. There is little information available regarding the distribution of the particles and their velocities relative to the gas phase near the grain surface or at the inflow boundary. Therefore, a limited parametric study of the parameters that characterize the particle injection was done, and the sensitivity of the two-phase calculations to these parameters was evaluated. The two-phase calculations were done for two different values of the particle injection velocities at the propellant surface. In one case, the particle velocity was taken to be 25% of the local gas velocity, and in the other case, it was 1% of the local gas velocity ($\approx$ no velocity). As for the particle injection at the inlet, two types of distributions were considered. In one case, the particulate mass flux at a radial location was assumed to be proportional to the local gas phase mass flux and in the other case, the particulate mass flux was assumed uniform along the radial direction. In both cases, the particle injection velocity at the inlet was assumed to be 75% of the local gas velocity.

The boundary conditions for the Lagrangian (particulate phase) calculations were as follows. The centerline was treated as a perfect reflecting surface; the propellant surface and the nozzle walls were treated as reflecting walls with a coefficient of restitution of 0.5. The inflow and outflow boundaries were considered as exit planes for the particles. The grid line at the cavity entrance was also treated as an exit surface for the particles; once the particles enter the cavity, they are likely to remain there because of gravity and large vertical accelerations during the motor flight. This is also computationally efficient; once a particle crosses this boundary, it does not have to be tracked anymore. If necessary, the cavity region can also be included in the two-phase calculations.

Single-Phase Calculations

The steady-state solutions for the continuous phase were obtained for geometries corresponding to both the initial time ($t = 0$) and one later ($t = 19$ s) burnback grain configurations.

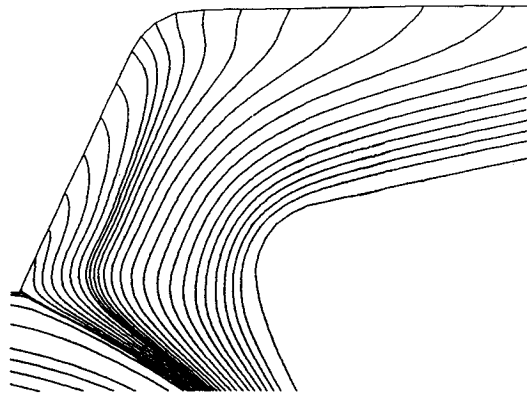

a) Streamlines

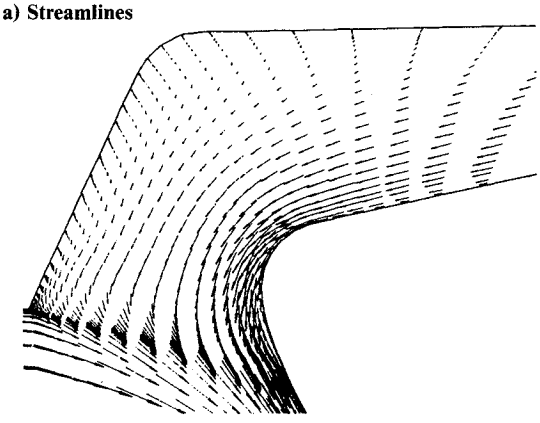

b) Velocity vectors

Fig. 4 Single-phase flow at initial grain configuration.

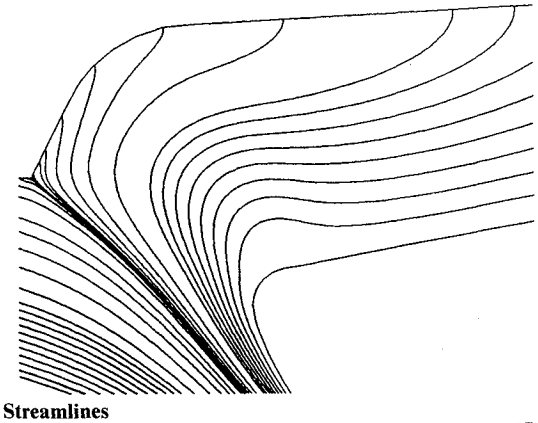

a) Streamlines

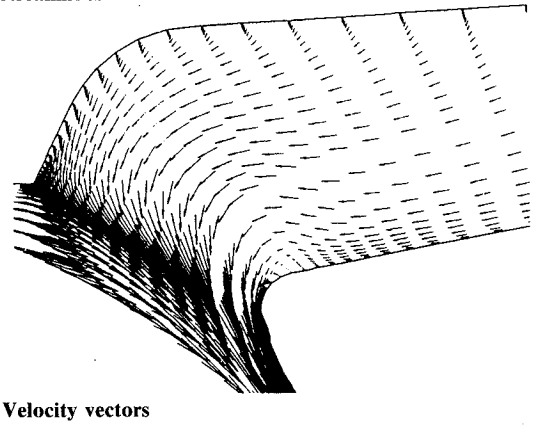

b) Velocity vectors

Fig. 5 Single-phase flow at 19-s burnback configuration.

For the initial configuration, the velocity vectors and the streamlines in the vicinity of the submerged nozzle cavity are shown in Fig. 4. For the 19-s burnback configuration, the corresponding plots are shown in Fig. 5. The influence of the

chamber flow on the cavity flow in the later burnback configuration can be seen by the presence of a small recirculation region in the nozzle entrance (nose) region. In the initial time configuration, the flow in the lower half of the cavity is almost parallel to the cavity wall, whereas, in the later burnback configuration, the chamber flow has changed the cavity flow by modifying the direction of the velocity vectors in the lower half of the cavity. This influence of the chamber flow on the cavity flow is, as explained before, due to the difference in the relative position of the grain surface with respect to the nozzle entrance in the initial and later burnback configurations. These differences in the flowfields suggest that the particles are more likely to enter the cavity in the later burnback configuration than in the initial grain configuration. For this reason, two-phase calculations were performed only for the 19-s burnback configuration.

Two-Phase Calculations

In view of the lack of information available regarding the particulate phase velocities and mass flux distribution at the propellant surface and the inflow boundary, three sets of two-phase flow simulations were performed for the 19-s burnback configuration. The particle injection conditions at the grain surface and at the inflow boundary were varied in these calculations. The differences in the two-phase effects (such as rate of particulate accumulation in the cavity and changes in the gas phase flowfield) were compared for these three cases in order to study the sensitivity of the calculated results to the assumptions made in the particulate injection.

Case 1

In this case, the particle injection velocity at the propellant surface was assumed to be 25% of the local gas velocity. At the inflow boundary, the particulate mass flux at all radial locations was assumed to be proportional to the local gas phase mass flux, and the particle injection velocity was assumed to be 75% of the local gas velocity. The gas phase Mach number contours in the nozzle region obtained from this two-phase flow simulation are compared with those obtained from the single-phase flow simulation in Fig. 6. As can be seen from Fig. 6, presence of the particulate phase results in an overall retardation of the gas phase in the nozzle region. Further, the Mach number contours for the two-phase simulation also exhibit a distinct distortion, which is a consequence of a larger concentration of the particulate phase in this region. The fact that the particles have a tendency to concentrate in this region

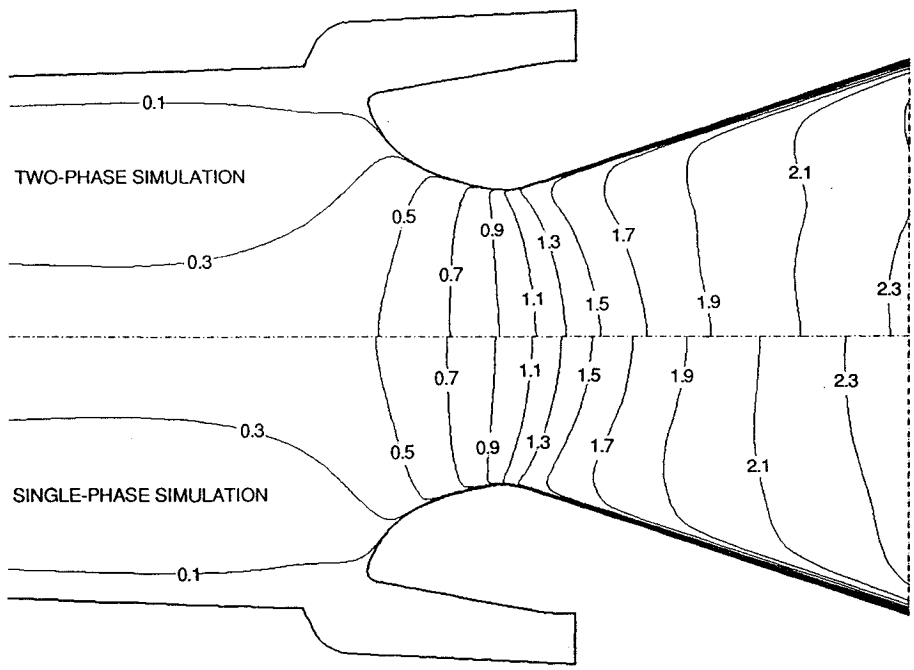

Fig. 6 Comparison of the Mach number contours in the nozzle region.

Fig. 7 Particle trajectories including the effect of gas phase turbulence on particle motion.

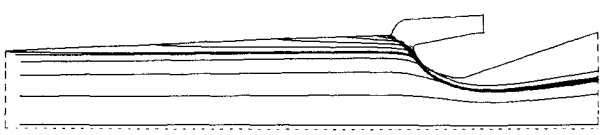

Fig. 8 Particle trajectories neglecting the effect of gas phase turbulence on particle motion.

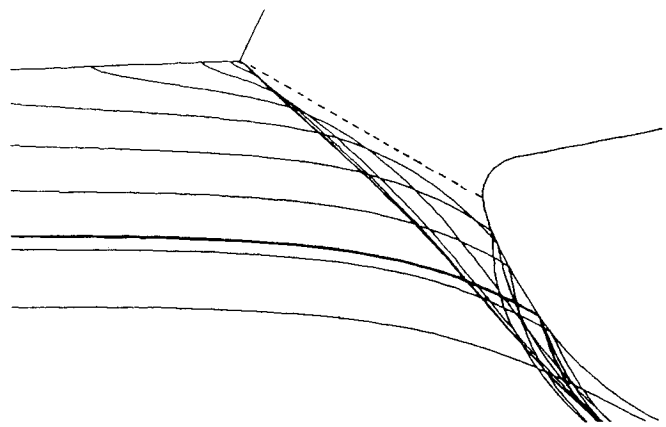

Fig. 9 Enlarged view of particle trajectories in the nozzle cavity entrance region.

can also be observed from Fig. 7, where the trajectories of the particles injected at selected locations are shown. Due to their large inertia, the particles cannot follow the gas phase streamlines in the rapidly expanding region of the nozzle, and this can be seen by the relatively straight trajectories, away from the nozzle walls in the diverging section. The wavy nature of the particle trajectories, especially near the porous wall, is due to the gas phase turbulence. An examination of the turbulence quantities in this region indicated that the fluctuating component of the velocity was of the same order as the mean velocity, and the randomness of these fluctuating velocities was responsible for the waviness of the particle trajectories. Figure 8 shows the particle trajectories computed neglecting the effect of gas phase turbulence on the particulate phase, and in Fig. 9 the enlarged view of these trajectories in the submerged nozzle entrance region is shown. The dashed line at the cavity entrance in Fig. 9 is a computational boundary in the particulate phase calculations, and all particles impinging on this boundary were assumed to enter the cavity and not tracked anymore. The trajectories obtained by neglecting the effect of gas phase turbulence on the particle motion can be seen to be smooth, reaffirming the earlier explanation of the role of gas phase turbulence on the particle trajectories. The reflection of the particles off the nozzle entrance wall (coefficient of restitution being 0.5) can also be seen in Fig. 9. The particles essentially seem to be following the gas phase streamlines in the chamber but not in the nozzle due to their large inertia as explained earlier. The calculations performed neglecting the effect of gas phase turbulence on the particle motion also indicated that, for this grain configuration, none of the particles enter the nozzle cavity. This indicates that the particle motion is highly influenced by the gas phase turbulence especially near the grain surface, and the effect of gas phase turbulence on particle motion needs to be further studied.

In the calculations performed, including the effect of the gas phase turbulence on the particulate motion, about 3.3% of the total particulate mass was found to enter the cavity. It should be noted that the strong flow out of the cavity at the 19-s burnback configuration could (depending upon the motor acceleration) potentially purge a significant portion of the particulates from the cavity and thereby reduce the slag accumulation rate. This effect is not accounted for in the present calculations since the particles were not tracked once they entered the cavity. Hence, the magnitude of the particulate accumulation is only qualitatively meaningful at this stage. However, it can be used effectively in parametric studies, such as those discussed below.

Case 2

The sensitivity of the slag accumulation rate to the assumed particulate injection conditions at the propellant surface was studied in this case. The particle injection velocity at the propellant surface was changed from 25 to 1% of the local gas velocity. The particulate injection conditions at the inflow boundary were identical to those in case 1. The gas phase flowfield did not change noticeably from that obtained in the previous case. About 3.5% of the total particulate mass was observed to enter the cavity, which is almost the same (statistically) as that in case 1, which indicates that the slag accumulation rate is not particularly sensitive to the particulate injection velocity at the grain surface.

Case 3

The objective of these calculations was to study the effect of particulate mass flux distribution assumed at the inflow boundary. In this case, the particle injection velocity at the propellant surface was the same as that in case 2. The particulate mass flux at the inflow was assumed to be uniform at all radial locations rather than proportional to the local gas phase mass flux. The particulate phase velocity at the inflow was still assumed to be 75% of the local gas velocity. No noticeable changes were observed in the gas phase flowfield compared with those obtained for the previous cases. This time, about 3.3% of the particulate mass was found to enter the cavity, which is about the same as that in case 2. This is because, even though the particle concentration near the propellant grain at the inlet is different from that in case 2, by the time the cavity region is reached, the particles are well dispersed and essentially follow the gas phase streamlines, much the same way as in case 2. These calculations confirm that the selected location of the inflow boundary is indeed sufficiently far upstream of the cavity region, and hence the effect of the assumptions/approximations made at this boundary on the flowfield in the region of interest would be minimal. More information regarding the distribution of the particulate phase is, however, necessary from experiments or other means in order to make accurate quantitative predictions of the two-phase effects.

Conclusions

An efficient Navier-Stokes analysis, combined with a coordinate space Lagrangian analysis, has been successfully used to simulate the two-phase flowfield in the submerged nozzle region of the Space Shuttle SRM. As the grain surface recedes with grain burnback, the chamber flow influences the flow in the cavity by causing the cavity flow to recirculate. The particle motion seems to be quite sensitive to the treatment of the effect of flow turbulence on the particulate phase. The particle accumulation in the submerged nozzle cavity does not appear to be particularly sensitive to the distribution of the particulate mass flux at the inflow boundary or to the particle injection velocity at the propellant surface. Although, in view of the lack of quantitative information about the particulate injection into the chamber, the particle accumulation rates obtained from the present calculations can only be of qualitative use, the analysis can be effectively used in parametric studies.

Acknowledgments

This research was supported by the Air Force Astronautics Laboratory under Contract F04611-86-C-0096 and by NASA George C. Marshall Space Flight Center under Contract NAS8-37255. The authors would also like to thank R. Harold Whitesides of SRS Technologies for his help in providing the geometric details of the grain configuration 19-s burnback and Mark Salita of Thiokol Corporation for the helpful discussions regarding the particulate size distribution in solid rocket motors.

References

[1]Sabnis, J. S., Giebeling, H. J., and McDonald, H., "Navier-Stokes Analysis of Solid Propellant Rocket Motor Internal Flows," *Journal of Propulsion and Power*, Vol. 5, No. 6, 1989, pp. 657–664.

[2]Sabnis, J. S., Madabhushi, R. K., Gibeling, H. J., and McDonald, H., "On the Use of k-ϵ Turbulence Model for Computation of Solid Rocket Internal Flows," AIAA Paper 89-2558, July 1989.

[3]Sabnis, J. S., Choi, S. K., Buggeln, R. C., and Gibeling, H. J., "Computation of Two-Phase Shear-Layer Flow Using an Eulerian-Lagrangian Analysis," AIAA Paper 88-3202, July 1988.

[4]de Jong, F. J., Sabnis, J. S., and McConnaughey, P. K., "A Combined Eulerian-Lagrangian Two-Phase Flow Analysis of SSME HPOTP Nozzle Plug Trajectories; Part I - Methodology," AIAA Paper 89-2347, July 1989.

[5]Sabnis, J. S., Gibeling, H. J., and McDonald, H., "Calculation of Solid Propellant Rocket Motor Internal Flow Field Using an Implicit Navier-Stokes Procedure," AIAA Paper 85-1625, July 1985.

[6]Jones, W. P., and Launder, B. E., "The Prediction of Laminarization with a Two-Equation Model of Turbulence," *International Journal of Heat and Mass Transfer*, Vol. 15, 1972, pp. 301–314.

[7]Briley, W. R., and McDonald, H., "Solution of the Multidimensional Compressible Navier-Stokes Equations by a Generalized Implicit Method," *Journal of Computational Physics*, Vol. 24, No. 4, Aug. 1977, pp. 372–397.

[8]Abbas, A. S., Kousa, S. S., and Lockwood, F. C., "The Prediction of the Particle Laden Gas Flows," *Proceedings of the 18th*

Symposium on Combustion, Combustion Inst., Pittsburgh, PA, 1981, pp. 1427–1438.

[9]Dukowicz, J. K., "A Particle-Fluid Model for Liquid Sprays," *Journal of Computational Physics*, Vol. 35, No. 2, April 1980, pp. 229–253.

[10]Gosman, A. D., and Ioannides, E., "Aspects of Computer Simulation of Liquid-Fueled Combustors," *Journal of Energy*, Vol. 7, No. 6, 1983, pp. 482–490.

[11]Thompson, J. F., "Composite Grid Generation Code for General 3-D Regions — the EAGLE Code," *AIAA Journal*, Vol. 26, No. 3, 1988, pp. 271–272.

[12]Oh, Y. H., "An Analytical Transformation Technique for Generating Uniformly Spaced Computational Mesh," NASA Langley Research Grant NSF 1087, Final Rept., Oct. 1978.

[13]Culick, F. E. C., "Rotational Axisymmetric Mean Flow and Damping of Acoustic Waves in a Solid Propellant Rocket," *AIAA Journal*, Vol. 4, No. 8, 1966, pp. 1462–1469.

[14]Price, E. W., "Combustion of Metallized Propellants," *Progress in Astronautics and Aeronautics: Fundamentals of Solid Propellant Combustion*, Vol. 90, AIAA, New York 1984, pp. 479–513.